Structural characterization of bimetallic nanomaterials with overlapping x-ray absorption edges

Laurent D. Menard,[1] Qi Wang,[2] Joo H. Kang,[1] Andrew J. Sealey,[1] Gregory S. Girolami,[1] Xiaowei Teng,[3] Anatoly I. Frenkel,[2] and Ralph G. Nuzzo[1]

[1]*Department of Chemistry, University of Illinois at Urbana–Champaign, Urbana, Illinois 61801, USA*

[2]*Department of Physics, Yeshiva University, New York, New York 10016, USA*

[3]*Department of Chemical Engineering, University of New Hampshire, Durham, New Hampshire 03824, USA*

(Received 15 January 2009; revised manuscript received 10 August 2009; published 28 August 2009)

We describe a data analysis method for extended x-ray absorption fine structure spectroscopy suitable for use with compounds of diverse form that contain overlapping absorption edges. This method employs direct concurrent analysis of the data—demonstrated here for cases involving two interfering metal edges—and does not utilize subtractive or data filtering strategies that have been previously used to address this challenge. Its generality and precision are demonstrated in analyses made on two model nanoscale samples: (1) a Ir-Pt nanoparticle system supported on γ-Al_2O_3 and (2) a hybrid system of Pt nanowires on which Au nanoparticles have been nucleated and grown at the nanowire tips, stacking faults, and twinning boundaries. The results obtained demonstrate the unique compositional and structural qualities of these two systems as well as the broader utility of the new x-ray absorption spectroscopy based protocol used to characterize them.

DOI: 10.1103/PhysRevB.80.064111 PACS number(s): 61.05.cj, 61.46.Df

I. INTRODUCTION

Nanomaterials are of considerable scientific and technological interest due to the nature of their nonbulklike optical, electronic, magnetic, and chemical (especially catalytic) properties.[1–3] An understanding of the dependence of these properties on and the precise atomistic details of composition and structure remains a critical challenge to progress in the field.[1–3] In metallic systems, an added level of complexity is often introduced by the inclusion of multiple elements whose arrangements in turn can lead to complex alterations of the nanomaterial properties.[4,5] How such sensitivities can be engineered by design (e.g., through the choice of metals, their relative composition, and the method of preparation) continues to attract considerable attention in materials research.[5–7] Advanced characterization techniques, especially those that can be used to elucidate structure and discriminate details about the local environments of individual atomic constituents, remain critical to the engineering of nanomaterials for technological applications.[4,8]

The current paper describes an advance in x-ray absorption spectroscopy (XAS), a powerful technique that provides element specific information on the electronic and structural properties of materials, applied to the characterization of two nanocrystalline model structures. In XAS, structural information (the coordination environment, bond distances, and structural disorder) can all be determined from fitting analysis of the extended x-ray absorption fine structure (EXAFS) spectra.[9–11] In multicomponent systems, such as a binary alloy, measurements at the absorption edges of both elements can provide rich information about homometallic and heterometallic bonding and coordination environments.[12–16] These analyses have been used to powerfully validate structural models of the bimetallic nanoparticles with pure alloy, core-shell, or layered character as specific examples.[13,17] Such analyses are complicated and indeed can fail for systems in which the component metals absorb x rays in the same spectral range (i.e., their signals in the postabsorption edge regions overlap). This is a particularly significant problem for metals that neighbor each other on the Periodic Table such as Ir, Pt, and Au, whose L_3 absorption edges are at 11 215, 11 564, and 11 919 eV, respectively. In this case, the edges are approximately 350 eV apart while the EXAFS oscillations in metals typically extend beyond 1000–1500 eV above the absorption edge, indicating that there is a considerable contribution from the EXAFS of the lower-energy element in the spectrum of the higher-energy element. Unless these overlapping contributions are disentangled, extracting structural information from the data via traditional data analysis strategies is inherently precluded.[18,19] Indeed, the proximity of the absorption edges in such cases prevents high precision analyses of structure for the lower-energy element, while the overlap of their EXAFS signals more generally impedes useful structural analyses for the higher-energy element.

The latter points are significant in that many multimetallic systems of fundamental interest and technological importance will contain some measure of spectral overlap. A prime example is in the area of heterogeneous catalysis where the use of multimetallic supported nanoparticles containing platinum group metals is ubiquitous. The modification of monometallic supported nanoparticle catalysts with secondary metals is a common strategy for impacting catalyst activity, selectivity, and stability.[20–23] For example, the addition of Re or Ir to a Pt/Al_2O_3 petroleum reforming catalyst significantly enhances its catalytic activity, increases the octane rating of the fuel product, and reduces deactivation of the catalyst due to coking.[20,24,25]

In this paper we present a strategy for performing fitting analyses of EXAFS data collected for bimetallic systems containing elements with overlapping absorption edges. This is accomplished by performing a first-nearest-neighbor (1NN) scattering path analysis in which the EXAFS data of each of the metal absorption edges are fit simultaneously, accounting for (1) the EXAFS of the lower-energy absorbing atom (e.g., Ir in Ir-Pt) at energies below the higher-energy (e.g., Pt in Ir-Pt) edge; (2) the continuation or "leakage" of lower-energy edge EXAFS signal into the region above the

higher-energy edge; and (3) the EXAFS at energies above the higher-energy edge attributable to the higher-energy absorbing atom. Application of the method to two very different model systems relevant to heterogeneous catalysis is presented in order to demonstrate its general applicability. These are (a) compositionally monodispersed Ir-Pt bimetallic nanoparticles prepared from a molecular cluster precursor supported on γ-Al_2O_3 and (b) Pt nanowires decorated by Au nanoparticles via a galvanic replacement reaction. We demonstrate in this paper the high precision of the method. These analyses provide unambiguous and self-consistent bases for characterizing the structural motifs present in these two systems: (a) a core-shell structure for the Ir-Pt nanoparticles and (b) discrete segregation of Au from Pt in the hybrid Pt-Au system.

II. DECONVOLUTION OF THE OVERLAPPING X-RAY ABSORPTION EDGES

The essence of the analysis strategy is demonstrated for an arbitrary bimetallic composition even though, for illustration purpose only, we use notation Ir and Pt for its constituent elements. Data analysis is done by a simultaneous fit of both Ir L_3 and Pt L_3 edges, which involve three contributions: (1) the Ir EXAFS in the Ir L_3 edge before the Pt L_3 edge; (2) the Ir EXAFS in the Pt L_3 edge; and (3) the Pt EXAFS in the Pt L_3 edge. Because (1) and (2) describe the same coordination environments they are strictly constrained mathematically. The analysis is done in R space and is limited to nearest-neighbor scattering paths, which are usually well isolated from longer scattering paths in the Fourier transforms of the EXAFS signal $\chi(k)$, where k is the photoelectron wave number. In this case, the EXAFS equations that are simultaneously fit are

$$\chi_{\mathrm{Ir\ edge}}(k_{\mathrm{Ir}}) = \frac{S_{0,\mathrm{Ir}}^2 N_{\mathrm{Ir}}}{k_{\mathrm{Ir}} R_{\mathrm{Ir}}^2} |f_{\mathrm{Ir}}^{eff}(k_{\mathrm{Ir}})| \sin\left[2k_{\mathrm{Ir}} R_{\mathrm{Ir}} - \frac{4}{3}\sigma_{\mathrm{Ir}}^{(3)} k_{\mathrm{Ir}}^3 + \delta_{\mathrm{Ir}}(k_{\mathrm{Ir}}) \right] e^{-2\sigma_{\mathrm{Ir}}^2 k_{\mathrm{Ir}}^2} e^{-2R_{\mathrm{Ir}}/\lambda_{\mathrm{Ir}}(k_{\mathrm{Ir}})} \quad (1)$$

and

$$\chi_{\mathrm{Pt\ edge}}(k_{\mathrm{Pt}}, k_{\mathrm{Ir}}) = \frac{S_{0,\mathrm{Pt}}^2 N_{\mathrm{Pt}}}{k_{\mathrm{Pt}} R_{\mathrm{Pt}}^2} |f_{\mathrm{Pt}}^{eff}(k_{\mathrm{Pt}})| \sin\left[2k_{\mathrm{Pt}} R_{\mathrm{Pt}} - \frac{4}{3}\sigma_{\mathrm{Pt}}^{(3)} k_{\mathrm{Pt}}^3 + \delta_{\mathrm{Pt}}(k_{\mathrm{Pt}}) \right] e^{-2\sigma_{\mathrm{Pt}}^2 k_{\mathrm{Pt}}^2} e^{-2R_{\mathrm{Pt}}/\lambda_{\mathrm{Pt}}(k_{\mathrm{Pt}})} + \frac{A S_{0,\mathrm{Ir}}^2 N_{\mathrm{Ir}}}{k_{\mathrm{Ir}} R_{\mathrm{Ir}}^2} |f_{\mathrm{Ir}}^{eff}(k_{\mathrm{Ir}})| \sin\left[2k_{\mathrm{Ir}} R_{\mathrm{Ir}} - \frac{4}{3}\sigma_{\mathrm{Ir}}^{(3)} k_{\mathrm{Ir}}^3 + \delta_{\mathrm{Ir}}(k_{\mathrm{Ir}}) \right] e^{-2\sigma_{\mathrm{Ir}}^2 k_{\mathrm{Ir}}^2} e^{-2R_{\mathrm{Ir}}/\lambda_{\mathrm{Ir}}(k_{\mathrm{Ir}})}, \quad (2)$$

where, indexed to the absorbing atom, S_0^2 is the passive electron reduction factor, N is the 1NN coordination number, R is the 1NN distance, σ^2 is the mean squared relative displacement of R, $\sigma^{(3)}$ is the third cumulant of the effective radial pair distribution function, $\lambda(k)$ is the photoelectron mean free path, and $f^{eff}(k)$ and $\delta(k)$ are the photoelectron scattering amplitude and phase, respectively.[9] The factor $A = \Delta\mu_{0,\mathrm{Ir}}/\Delta\mu_{0,\mathrm{Pt}}$, where $\Delta\mu_{0,\mathrm{Ir}}$ and $\Delta\mu_{0,\mathrm{Pt}}$ are the changes in the absorption at the edge steps, is necessary because the extraction of $\chi(k)$ includes a normalization to these edge steps. Therefore it follows that, if the Ir L_3 and Pt L_3 edge steps are different in magnitude, the difference in this scaling factor between the Ir EXAFS in the Ir L_3 edge and the Ir EXAFS in the Pt L_3 edge needs to be accounted for. The nonlinear least-squares fitting of experimental data to Eqs. (1) and (2) should be done concurrently to the overlapping L_3 edges and can be achieved using available EXAFS analysis tools. For this work, the interface programs ATHENA and ARTEMIS,[26] which implement the FEFF6 and IFEFFIT codes, were used.[27,28]

The final complication in the analysis is that the Pt EXAFS oscillations as extracted from the experimental absorption edge are described as a function of a single wave number, k_{Pt}, so the real functional dependence of the data in this range on both k_{Pt} and k_{Ir}, which are referenced to different threshold energies, needs to be accounted for.[29] A standard EXAFS analysis includes an empirical correction for the photoelectron energy E_0, to which the theoretical k-dependent scattering functions are referenced. In this analysis, the correction factors $\Delta E_{0,\mathrm{Ir}}$ and $\Delta E_{0,\mathrm{Pt}}$ are varied as usual for the Ir EXAFS in the Ir L_3 edge and the Pt EXAFS in the Pt L_3 edge, respectively. The correction to the threshold energy (in eV) for the Ir EXAFS in the Pt L_3 edge is then defined as $\Delta E_{0,\mathrm{Ir}} - (349 + \Delta E_{0,\mathrm{Pt}})$, where 349 eV is the difference between the empirical threshold energies, and its purpose is to correct the energy grid in k space for the Ir EXAFS in the Pt L_3 edge. Such a large energy origin shift is necessary in this method since it accounts for a unique $k=0$ reference point for the Ir EXAFS extending beyond the Pt edge when the Pt edge EXAFS is transformed to k space. The exact value to use (here 349 eV) will depend on the E_0 values that are used in the edge subtraction of the EXAFS spectra. The general rule of thumb that $\Delta E_{0,\mathrm{Ir}}$ and $\Delta E_{0,\mathrm{Pt}}$ should be within the range of approximately ± 10 eV to indicate a reasonable theoretical fit is still an appropriate guideline.

The end result of this analysis is one in which both the Ir and Pt EXAFS data are analyzed over their full energy (or k) ranges (with a small gap of ~ 1.5 Å^{-1} centered on the Pt L_3 edge). The ability to carry out a direct fit of the Ir EXAFS that overlaps the Pt L_3 edge significantly minimizes errors in the Pt fitting results. These benefits are not similarly endowed when other approaches are used to account for edge overlap (see below). The S_0^2 values required for the analysis are determined from appropriate bulk standards and A is a constant determined from the absorption edge steps. As such, a total of ten variables are used to generate the two-edge fit. This value is well below the information limit of the data.

In the examples described below, the theoretical scattering functions used in Eqs. (1) and (2) were calculated by FEFF6 for bulk metals (fcc Pt, Ir, and Au) as well as bulk PtO_2 oxide (for the Au-Pt system). All data were k^2-weighted for the fitting analysis. We note that, for the Ir-Pt sample, it is not possible to fit the Ir-Ir, Ir-Pt, and Pt-Pt scattering paths independently with high confidence due to the closely matched lattice parameters and similar backscattering amplitudes and phases of Pt and Ir. Thus, in this instance, the variables in-

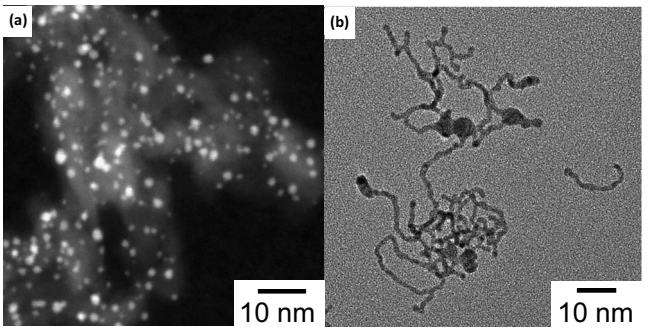

FIG. 1. Representative electron microscopy images of the two model systems described in this work. (a) Annular dark field scanning transmission electron microscopy image of 10 wt % Ir-Pt nanoparticles deposited on γ-Al_2O_3. (b) Transmission electron microscopy (TEM) image of Pt-Au nanowire-particle hybrids.

dexed to the Ir and Pt absorbers are ones characteristic of scattering arising from both Pt and Ir neighbors. A similar consideration also holds for the Pt-Pt, Pt-Au, and Au-Au scattering paths for the data obtained from the Pt-Au sample.

III. EXAMPLES: Ir-Pt AND Au-Pt BIMETALLIC SYSTEMS

As noted in Sec. I, the ability to accurately determine the structure of bimetallic systems is particularly important in the characterization of nanomaterials in order to understand behavior that may differ from that observed in the bulk materials and that potentially impacts their physical and chemical properties. We investigate here two different bimetallic nanoscale systems of interest as models of heterogeneous catalysts. The first was a sample of Ir-Pt bimetallic nanoparticles prepared on a high-surface-area γ-Al_2O_3 support using a bimetallic cluster precursor.[30] Analytical electron microscopy revealed these supported nanoparticles to be highly monodisperse $(1.7 \pm 0.5$ nm) with a composition $(53\% \pm 5\%$ Ir) consistent with the stoichiometry of the cluster precursor, $Ir_3Pt_3(\mu\text{-}CO)_3(CO)_3(\eta\text{-}C_5Me_5)_3$ [Fig. 1(a)].[30] The second system was a sample of Pt nanowires decorated with Au nanoparticles ("Pt-Au hybrid") prepared by means of a galvanic replacement reaction between Pt nanowires and $AuCl_3$. The latter reaction leads to the nucleation and growth of Au nanoparticles localized along the ends and length of the Pt nanowires. The procedures used to control the particle growth in the Pt-Au hybrids are described in greater detail in the literature.[31] The resulting structures, short Pt nanowire segments with an average cross-sectional diameter of 2.3 ± 0.2 nm bearing Au nanoparticles with an average diameter of 4.5 ± 0.8 nm, are shown in Fig. 1(b).[31]

In order to best demonstrate the feasibility and advantages of the approach described in Sec. II we also analyzed the EXAFS spectra for metallic Ir and Pt standards collected from the isolated standards and then from the stacked standards. These results provide a high level of confidence in the ability of this analysis method to be easily implemented in the characterization of bimetallic nanomaterials and are presented first in Sec. IV below.

X-ray absorption spectra were collected at beamline 33-BM at the Advanced Photon Source at Argonne National Laboratory and at beamline X18B at the National Synchrotron Light Source at Brookhaven National Laboratory. For measurements of the supported Ir-Pt nanoparticles (we used pressurized powder pellets as specimens), spectra were collected in transmission modes at the Ir L_3 edge from 200 eV below the edge to 310 eV above the edge and at the Pt L_3 edge from 200 eV below the edge to 1200 eV above the edge. The highest-energy values for the Ir L_3 and Pt L_3 spectra were limited by the onset of the Pt L_3 and Ir L_2 absorption edges, respectively. Specimens of the Pt-Au hybrids were prepared by drop casting a concentrated suspension of nanowires in chloroform onto Kapton tape, forming a uniform film that was then mounted in the beam at a 45° angle to allow simultaneous fluorescence and transmission measurements. Energy ranges similar to those used for the Ir-Pt sample were scanned for the Pt-Au sample, with energy limits determined by the positions of the Pt and Au edges.

Measures were taken to reduce Ir-Pt nanoparticles and prevent oxidation during the measurements by performing the experiments under a 4% H_2 (balance He) atmosphere, as described elsewhere; spectra were collected with the sample cooled to 215 K.[30] Spectra of the Pt-Au hybrid nanostructures were acquired under an ambient atmosphere at room temperature. For both samples, multiple spectra were measured at each edge for signal averaging.

IV. RESULTS

In order to illustrate the effect of the overlap of Ir L_3 EXAFS with the Pt L_3 absorption edge, a simple experiment was performed in which the respective L_3 absorption edges were measured for a Pt foil (4 μm) and an Ir bulk standard of Ir black (i.e., finely divided metallic Ir) diluted with C black, both of which exhibited an edge step close to $\mu\Delta x = 1$. Data were collected from 200 eV below the respective absorption edges up to 1500 eV above the edges. Then the standards were stacked and the truncated Ir L_3 edge and the Pt L_3 edge with overlapping Ir EXAFS were measured as detailed in Sec. II.

These data are shown in Fig. 2 in order to illustrate the characteristics of the absorption edge overlap. Figure 2(a) shows the normalized absorption spectra (L_3 edges) for the Ir and Pt bulk metallic standards measured individually and in the stacked configuration. The spectra are normalized to ensure that they overplot, facilitating a direct comparison. This is necessary due to slight changes in the un-normalized spectra between measurements resulting from changes in the beam brightness, detector efficiencies, or slight differences in the sample thickness as a result of repositioning the standards for each of the measurements. Because the edge steps for both edges were close to $\mu\Delta x = 1$ the normalized data provide an accurate representation of the magnitudes of the EXAFS oscillations in both edges and the effects of edge overlap. Specifically, it is evident from Fig. 2(a) that the magnitude of the Ir L_3 EXAFS is still significant at energies above the Pt L_3 absorption edge. This is also manifested in the differences between the Pt L_3 EXAFS spectra of the iso-

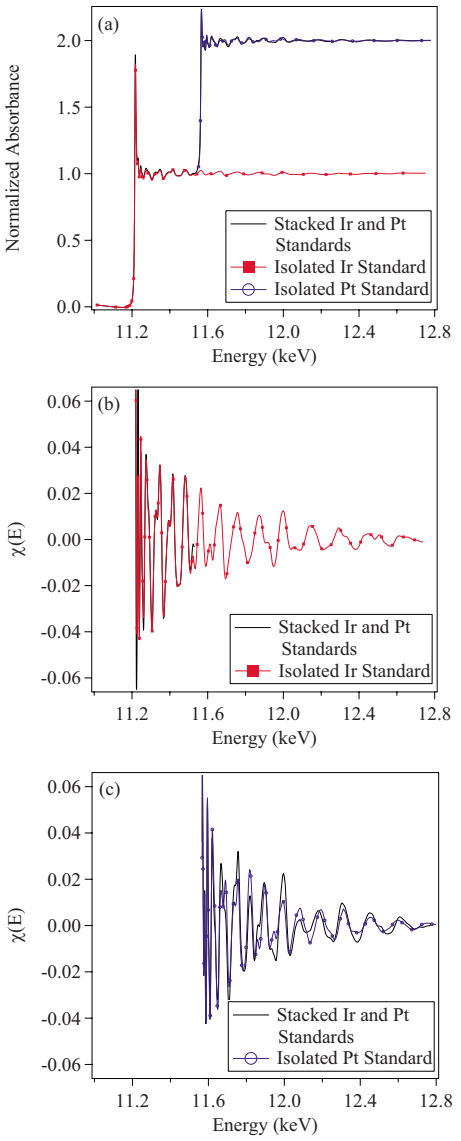

FIG. 2. (Color online) Plots in energy space of the spectra collected from the isolated metallic Ir and Pt standards compared to the spectra collected from the stacked standards. (a) Normalized absorption spectra at the Ir and Pt L_3 edges. (b) Background-subtracted Ir L_3 spectra. (c) Background-subtracted Pt L_3 spectra.

lated Pt metallic standard and the stacked standards. These effects are more dramatically illustrated by subtraction of the absorption edge backgrounds to yield the isolated EXAFS oscillations, $\chi(E)_{\mathrm{Ir}}$ and $\chi(E)_{\mathrm{Pt}}$, shown in Figs. 2(b) and 2(c), respectively. This background subtraction was done with a cubic spline fit to the absorption edge using the AUTOBK code implemented in ATHENA with an R_{bkg} value of 1.2 Å. R_{bkg} is a constraint on the spline fit that minimizes EXAFS contributions in R space below this value (i.e., low-frequency components).[32] The $\chi(E)_{\mathrm{Ir}}$ spectra shown in Fig. 2(b) show the overlap of the Ir EXAFS near the absorption edge and also illustrate the large amount of high quality data that would not be utilized if the portion of the Ir EXAFS that overlaps with the Pt L_3 edge is not analyzed. The $\chi(E)_{\mathrm{Pt}}$ spectra shown in Fig. 2(c) illustrate the significant convolution of the Pt L_3 EXAFS due to the overlap of the Ir L_3 EXAFS.

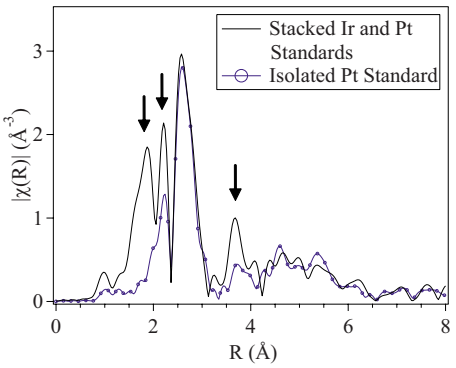

FIG. 3. (Color online) Comparison of the EXAFS spectra of a Pt foil standard and the Pt foil stacked with an Ir black standard. The spectra are plotted as the Fourier transform magnitudes of the k^2-weighted data, $\chi(k)$, over the range $k=2-18$ Å^{-1}. The contributions from overlap of the Ir EXAFS with the Pt L_3 edge are indicated by the arrows.

Figure 3 presents a further comparison of the Pt L_3 EXAFS spectra both with and without the Ir EXAFS overlap contribution. These data are presented as the Fourier transform magnitudes of the k^2-weighted $\chi(k)$ functions transformed over the range $k=2-18$ Å^{-1} ($R_{\mathrm{bkg}}=1.2$ Å). The contribution of the Ir EXAFS overlap is obvious and is highlighted by the arrows in the figure. The contribution from the first shell Ir scattering, which is marked by the two leftmost arrows in the figure, appears deceptively similar to the contribution from a low-atomic-number scatterer such as oxygen or sulfur with a bond length shorter than the metal-metal bonds. The contribution marked by the arrow on the right of the figure is due to longer Ir scattering paths (single and multiple scatterings) and again shows a marked shift to lower R values. As the analysis is limited to a first shell fit, this latter contribution can be ignored as it does not overlap with the first shell and so does not affect the fits presented in this paper.

The appearance of the Ir overlap contribution at low R values in Fig. 3 can be readily explained as an effect of the distortion of the Ir EXAFS oscillations when the Pt L_3 EXAFS spectrum is transformed from energy space to k space using the Pt L_3 threshold energy. A shell of scatterers at a distance R gives rise to EXAFS oscillations in k space that follow a damped sine wave, whose period (to first order) is inversely related to R. In energy space, however, the spacing between successive oscillation extrema increases, and thus the Ir EXAFS oscillations in the Pt edge will be characterized by relatively large period. If these oscillations are treated as if they were part of the Pt EXAFS spectrum and are converted to k space using the Pt L_3 threshold energy, they will appear to arise from a shell of scatterers at an internuclear distance that is much shorter than the actual distance. In other words, the lower-frequency character of the Ir $\chi(k)$ function at the Pt edge is transformed as a low R peak. Of importance to note here is that, whereas the phase and period of the distorted Ir EXAFS may mimic a low-Z scatterer, the amplitude behavior due to $f^{eff}(k)$ is very differ-

TABLE I. Fitting analysis results for metallic Ir and Pt standards collected individually (leftmost column of results) and in stacked configuration (remaining columns of results) using various strategies. See text for details. Data ranges used for the fitting analyses are provided in the table. All data were k^2 weighted. All results are for spectra collected with the sample at room temperature.

Parameter	Isolated Ir, Pt standards	Stacked Ir, Pt standards simultaneous two-edge fit	Ir edge only	Pt only $R_{bkg}=1.2$	Pt only $R_{bkg}=1.2$ restricted R range	Pt with Pt-O contribution
N_{Ir} (defined)	12	12	12			
$S^2_{0,Ir}$	0.83 ± 0.04	0.81 ± 0.07	0.75 ± 0.15			
$\Delta E_{0,Ir}$ (eV)	8.7 ± 0.8	7.3 ± 1.6	7.3 ± 2.4			
R_{Ir} (Å)	2.707 ± 0.005	2.70 ± 0.01	2.70 ± 0.04			
σ^2_{Ir} (Å^2)	0.0034 ± 0.0001	0.0034 ± 0.0003	0.003 ± 0.002			
$\sigma^{(3)}_{Ir}$ (Å^3)	0.00002 ± 0.00003	0.00001 ± 0.00007	0 ± 0.0007			
Ir L_3 k range (Å^{-1})	2.0–18.0	2.7–18.6	2.7–8.7			
Ir L_3 R range (Å)	1.8–3.0	1.2–3.1	1.2–3.1			
N_{Pt} (defined)	12	12		12	12	12
$S^2_{0,Pt}$	0.86 ± 0.03	0.88 ± 0.09		0.94 ± 0.21	0.85 ± 0.21	0.83 ± 0.31
$\Delta E_{0,Pt}$ (eV)	8.5 ± 0.6	7.5 ± 1.7		10.7 ± 3.6	9.9 ± 4.6	7.8 ± 8.6
R_{Pt} (Å)	2.768 ± 0.004	2.76 ± 0.01		2.77 ± 0.03	2.77 ± 0.04	2.76 ± 0.07
σ^2_{Pt} (Å^2)	0.0049 ± 0.0001	0.0048 ± 0.0004		0.0051 ± 0.0008	0.0045 ± 0.0009	0.004 ± 0.002
$\sigma^{(3)}_{Pt}$ (Å^3)	0.00003 ± 0.00003	0 ± 0.0001		0 ± 0.0002	0 ± 0.0002	0 ± 0.0005
Pt L_3 k range (Å^{-1})	2.0–18.0	2.7–16.0		2.7–16.0	2.7–16.0	2.7–16.0
Pt L_3 R range (Å)	1.8–3.0	1.2–3.0		2.3–3.0	2.3–3.0	1.2–3.0
A (defined)	NA	0.959				
$N_{Pt\text{-}O}$						3.3 ± 2.2
$R_{Pt\text{-}O}$ (Å)						2.10 ± 0.04
$\sigma^2_{Pt\text{-}O}$ (Å^2)						0 ± 0.003
Independent points	11.8, 11.8 (Ir, Pt)	21.9	7.1	5.7	5.7	14.8
Variables	5, 5 (Ir, Pt)	10	5	5	5	8
Reduced χ^2	459, 290 (Ir, Pt)	1183	916	3592	4586	38192
R factor	0.003, 0.002 (Ir, Pt)	0.002	0.002	0.0007	0.0008	0.05

ent. It is therefore possible to fit overlapping Ir EXAFS and Pt-low-Z scattering contributions in uniform bimetallic systems when such scatterers are present in analytically viable concentrations.[9,11]

The qualitative comparison of the EXAFS spectra measured for the bulk metallic Ir and Pt standards in isolated and stacked configurations illustrates the difficulties posed by the overlap of absorption edges. A fitting analysis of these spectra using the method described in this paper demonstrates the advantages of this analysis, quantitatively, over other strategies that attempt to account for the absorption edge overlap. The values for the structural parameters of the isolated metallic standards determined from the fitting analysis of data ($k=2-18$ Å^{-1}) are presented in Table I. Immediately to the right of these data in Table I are the results obtained from the stacked standards using the simultaneous two-edge fitting analysis described above. We note that fitting the overlapping absorption edges measured from the stacked standards using the method described in Sec. II yields identical values for the fitting parameters as those obtained by fitting the absorption spectra collected from the standards individually within the uncertainties. A comparison of the theoretical fits to the measured spectra for the stacked standards is shown in Fig. 4 as both the Fourier transform magnitude [R space; Figs. 4(a) and 4(b)] and the real component of the inverse Fourier transform taken over the fitting range in R space [Figs. 4(c) and 4(d)]. The contributions from both the Pt-M (M=Ir or Pt) and Ir-M scattering paths are shown in the Pt L_3 spectra to convey the relative importance of these two contributions. The inverse Fourier transform plots represent the phase and amplitude of the individual paths used in the fit. The uncertainties in the structural parameters obtained by fitting the stacked standards are slightly greater than those obtained by fitting the isolated standards as are the statistical figures of merit of the fit quality (reduced χ^2, R factor). This is consistent with the reduced range of data available for analysis and to correlations between the Ir-M and Pt-M scattering contributions that are introduced by the absorption edge overlap.

The advantages of this approach to edge deconvolution and fitting analysis are best illustrated by comparing the results to those obtained using alternative strategies. Because the Ir L_3 absorption edge is the lowest-energy L edge of the

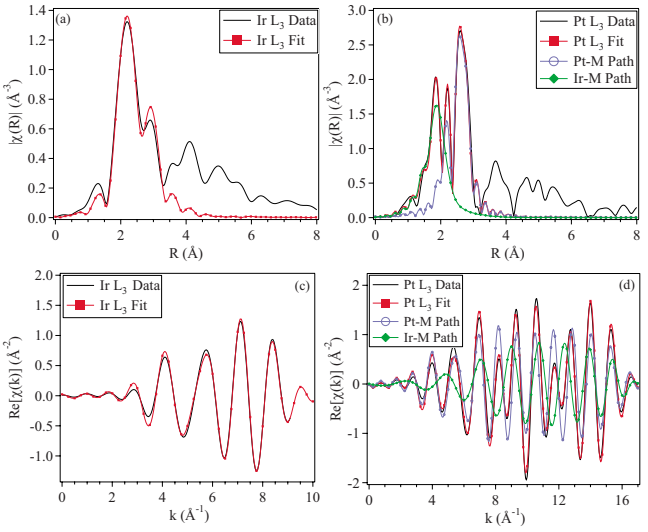

FIG. 4. (Color online) Comparison of the data and fit of the stacked Ir and Pt metallic standards. (a) Fourier transform magnitude of the Ir L_3 data and fit (k=2.7–8.7 Å^{-1}, R=1.2–3.1 Å, k^2 weighted). (b) Fourier transform magnitude of the Pt L_3 data and fit (k=2.7–16.0 Å^{-1}, R=1.2–3.0 Å, k^2 weighted) with the contributions of the individual paths represented. (c) Real component of the inverse Fourier transform of Ir L_3 data and fit. (d) Real component of the inverse Fourier transform of Pt L_3 data, fit, and paths.

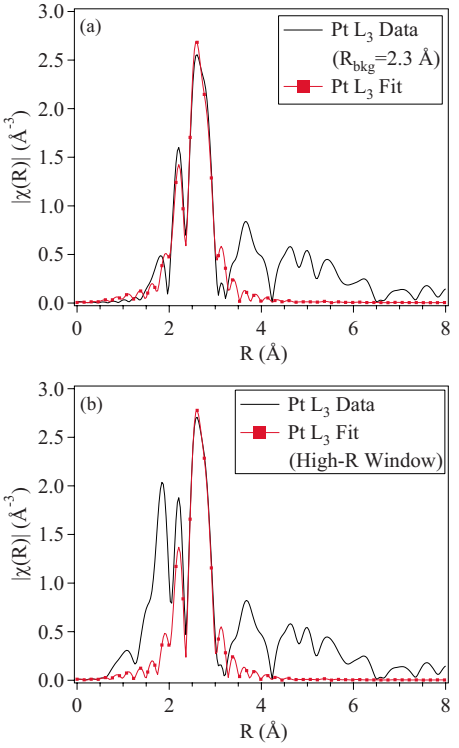

FIG. 5. (Color online) Comparison of the data and fits obtained when attempting to fit the Pt-M scattering path by minimizing the contribution of the Ir-M overlap. (a) Fourier transform magnitude of the Pt L_3 data after removing the low-frequency components by performing the background subtraction with a large R_{bkg} value (R_{bkg}=2.3 Å) and the resulting fit (k=2.7–16.0 Å^{-1}, R=2.3–3.0 Å, k^2 weighted). (b) Fourier transform magnitude of the Pt L_3 data and fit performed by constraining the R range to filter out the Ir-M overlap contribution (k=2.7–16.0 Å^{-1}, R=2.3–3.0 Å, k^2 weighted).

Ir and Pt constituents, it is spectrally "pure" with no components from other absorption edges. However, fairly large uncertainties are expected in a fitting analysis of the data truncated at approximately k=8.7 Å^{-1} by the Pt L_3 edge. This is indicated in Table I where a comparison of the simultaneous two-edge analysis to the analysis that fits solely the Ir L_3 EXAFS demonstrates the advantages gained by increasing the Ir L_3 data range.

Two related strategies might be implemented in an attempt to fit the Pt L_3 EXAFS without fitting the Ir-M EXAFS by minimizing the contribution of this latter component. One strategy is to use a large R_{bkg} value in the background subtraction algorithm to minimize the low-frequency components in the spectrum. This strategy was attempted for the Pt L_3 EXAFS collected from the stacked samples and a value of R_{bkg}=2.3 Å was found to be optimal for reducing the Ir-M contribution while not severely distorting the Pt-M contribution. A range of R_{bkg} values was attempted and both smaller and larger values led to poorer fits as assessed by the uncertainties in the structural parameters and by the statistical figures of merit. The results of this analysis are given in Table I and a graphical comparison of the data and fit is presented in Fig. 5(a). If the Ir-M contribution is not minimized by the background subtraction, but instead the data are analyzed over an R range that does not include the low-R Ir-M EXAFS (essentially Fourier filtering the data) then similar results are obtained. The difference between this latter strategy and the strategy employing a more aggressive background subtraction is that there is no risk of distortions to the Pt-M EXAFS when merely restricting the R range. A comparison between the data and the fit obtained with this strategy is shown in Fig. 5(b). While the values obtained by these alternative methods are close to those determined using the simultaneous fitting strategy they are obviously of much lesser quality and usefulness with regard to both accuracy and precision.

One final test was employed in which the low-R contribution was fit not with the Ir-M EXAFS but with a low-Z scattering path, here Pt-O, to investigate chemical sensitivity of this fitting approach when metal nanoparticles, prone to oxidation, are studied. The resulting fit is compared to the data in Fig. 6 and qualitatively appears to be a relatively poor fit. Moreover, the structural parameter results and statistical figures of merit shown in Table I are in agreement with this assessment. The large Pt-O coordination number ($N_{Pt\text{-}O}$ = 3.3 ± 2.2) is greater than that of the bulk oxide ($N_{Pt\text{-}O}$ = 2.0) and is highly correlated with the mean squared relative displacement, $\sigma^2_{Pt\text{-}O}$, which has a best fit value of $\sigma^2_{Pt\text{-}O}$ = 0 ± 0.003 Å^2. Additionally, the reported Pt-O half scattering path length ($R_{Pt\text{-}O}$=2.10 ± 0.04 Å) is approximately 0.10 Å longer than typical Pt-O bonds in oxides.[33] Clearly, the data are inadequately fit by introducing a Pt-O scattering path in this example. However, in situations where the Ir-M EXAFS that overlaps with the Pt L_3 edge is of lower magnitude, the difference between the data and a fit using a Pt-O path is expected to decrease and the amplitude parameters, $N_{Pt\text{-}O}$ and $\sigma^2_{Pt\text{-}O}$, to assume more reasonable values. This

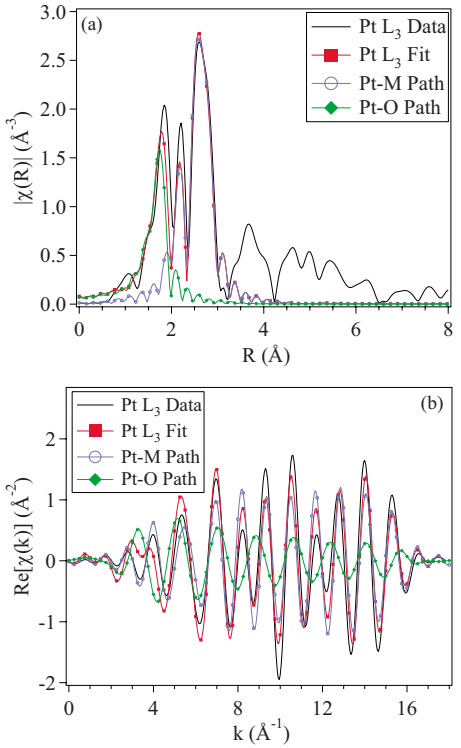

FIG. 6. (Color online) Comparison of the data, fit, and path contributions when attempting to fit the low-R portion of the spectrum with a Pt-O scattering contribution (k=2.7–16.0 Å^{-1}, R =1.2–3.0 Å, k^2 weighted). (a) Fourier transform magnitude. (b) Real component of the inverse Fourier transform.

leaves open the possibility of concluding the presence of an erroneous oxide contribution (albeit one with a questionable Pt-O bond distance) if the Ir-M EXAFS overlap is ignored in the analysis of nanoalloys. This error should be easily avoided when one considers a comparison of the phase and amplitude of the Pt-O path in Fig. 6(b) with that of the Ir-M overlap contribution in Fig. 4(d). These data clearly indicate differences significant enough to differentiate the two contributions, particularly with the information afforded by the Ir L_3 absorption edge.

The above demonstration of the edge overlap deconvolution is necessary to validate the application of this EXAFS analysis method to the characterization of bimetallic nanomaterials. Representative TEM images of the two nanoscale samples investigated are shown in Fig. 1. It is evident that these metallic structures are very different. The Ir-Pt system contains particles of roughly the same size, whereas the Au-Pt system contains a system of two different types of objects: the nanowires (Pt rich) and nanoparticles (Au rich).[31] As verified by energy-dispersive spectroscopy analysis, both systems are compositionally monodisperse and thus suitable for EXAFS investigation.[30,31]

The sample of supported Ir-Pt nanoparticles on γ-Al_2O_3 is well suited for a demonstration of the multiedge fitting analysis applied to the elucidation of nanomaterial structure. The high concentration of nanoparticles and the 1:1 Ir-Pt compositional ratio ensure high quality data at both absorption edges. Additionally, the narrow distributions of nanoparticle size and elemental composition ensure that the EXAFS

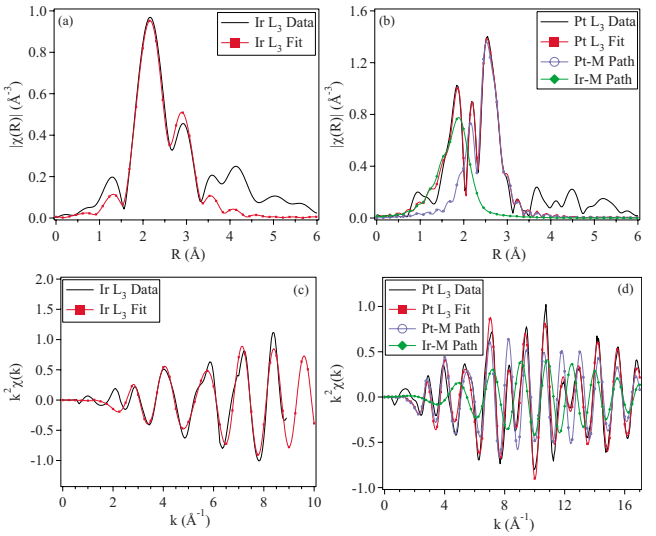

FIG. 7. (Color online) Comparison of the data and fit of the Ir-Pt nanoparticles on γ-Al_2O_3 under a H_2 atmosphere measured at 215 K at the Ir L_3 and Pt L_3 absorption edges. (a) Fourier transform magnitude of the Ir L_3 data and fit (k=2.7–8.6 Å^{-1}, R =1.2–3.1 Å, k^2 weighted). (b) Fourier transform magnitude of the Pt L_3 data and fit (k=2.7–17.2 Å^{-1}, R=1.3–3.0 Å, k^2 weighted) with the contributions of the individual paths represented. (c) k-space plot of Ir L_3 data and fit. (d) k-space plot of Pt L_3 data, fit, and paths.

data are representative of an intraparticle structural motif and not an ensemble average of disparate nanoparticle populations.[34] The Fourier transform magnitudes of the Ir L_3 and Pt L_3 EXAFS spectra of the Ir-Pt/ γ-Al_2O_3 nanoparticles are shown in Figs. 7(a) and 7(b), along with the fits simultaneously performed at the two absorption edges. These data and fitting results are also shown in k space in Figs. 7(c) and 7(d). The fitting analysis using the three contributions described above is clearly of high quality, an assessment supported by the low relative uncertainties of the fit results and the statistical parameters, which are provided in Table II. The S_0^2 values used in the fits were those determined using Ir and Pt bulk standards and were 0.83 and 0.86, respectively. The edge normalization factor A was constrained to be 1.0, as determined from the ratio of the Ir L_3 and Pt L_3 absorption edges.

The Ir and Pt first shell coordination numbers (9.3 ± 0.5 and 7.2 ± 0.6, respectively) are less than the bulk fcc value of 12 owing to the small size of the nanoparticles and the relatively large numbers of surface atoms with small coordination numbers. The most nontrivial result obtained using the fitting analysis relates to the difference between these coordination numbers. A homogeneous alloy would exhibit identical coordination environments for the Ir and Pt atoms in clusters of this type. The differences in the coordination numbers reflect the segregation of different atomic species to the surfaces and cores of the particles, consistent in this case with an Ir rich core surrounded by a Pt rich shell. The overall coordination number is defined as the average coordination numbers of the individual components in the bimetallic system, weighted by their relative abundances. This value (8.3 ± 0.8) is in close agreement with the value estimated for

TABLE II. Results of the fit to $\chi(R)$ of the Ir and Pt L_3 EXAFS using FEFF and FEFFIT for the Ir-Pt nanoparticles on γ-Al_2O_3, accounting for the overlap of the Ir EXAFS with the Pt L_3 absorption edge.

Ir parameters		Pt parameters	
N_{Ir}	9.3 ± 0.5	N_{Pt}	7.2 ± 0.6
$\Delta E_{0,Ir}$ (eV)	5.7 ± 0.7	$\Delta E_{0,Pt}$ (eV)	7.3 ± 1.3
R_{Ir} (Å)	2.687 ± 0.007	R_{Pt} (Å)	2.74 ± 0.01
σ^2_{Ir} (Å^2)	0.0047 ± 0.0002	σ^2_{Pt} (Å^2)	0.0057 ± 0.0003
$\sigma^{(3)}_{Ir}$ (Å^3)	0 ± 0.00005	$\sigma^{(3)}_{Pt}$ (Å^3)	0.00008 ± 0.00008
Ir L_3 k range (Å^{-1})	2.7–8.6	Pt L_3 k range (Å^{-1})	2.7–17.2
Ir L_3 R range (Å)	1.2–3.1	Pt L_3 R range (Å)	1.3–3.0

Independent points	22.3
Variables	10
Reduced χ^2	133
R factor	0.004

nanoparticles with an average diameter of 1.7 nm and a truncated cuboctahedral geometry (N=8.2), a model consistent with the electron microscopy results.[35]

It is also structurally significant that the values of the mean squared relative displacements, σ^2_{Ir} and σ^2_{Pt}, are about two times larger than those observed in the bulk materials at the same temperature (0.0028 ± 0.0001 and 0.0037 ± 0.0001 Å^2 for Ir and Pt, respectively). This behavior is generally observed in metal nanoparticles as the percentage of surface atoms increases, but the effect is especially large in the present case due to the fact that the internuclear distance R is being used to fit scattering from both homometallic and heterometallic neighbors.[35,36] Finally, the EXAFS analysis provides a measure of the effective first-nearest-neighbor bond distances with precision on the order of 0.01 Å. The latter data show that both the R_{Ir} and R_{Pt} distances are contracted from the bulk values of Ir and Pt (2.704 ± 0.005 and 2.764 ± 0.002 Å, respectively, at 215 K). Although bond relaxations of this magnitude are commonly observed in metal nanoparticles due to their lower coordination environment,[35,36] we note that the expected Ir-Ir bond length contraction should be even greater than that reported by R_{Ir} because this value is a weighted average of the relatively shorter Ir-Ir bond distances and the relatively longer Ir-Pt bond distances, contributions that we cannot differentiate. Conversely, $R_{Pt\text{-}Pt}$ is expected to be greater than the measured R_{Pt} due to the contribution of Ir neighbors to R_{Pt}, and we cannot, strictly speaking, claim the contraction of Pt-Pt distances relative to the Pt bulk, as we can in the case of the Ir-Ir bond.

The Pt-Au hybrid sample provides a second—and in this case a more challenging—test of the analysis method. The signal is lower for this sample, particularly at the Au L_3 edge due to the fact that Au is a minor elemental component in the sample. The data also reveal that there is a non-negligible contribution from Pt-O scattering (one arising because the sample was measured in ambient atmosphere and was therefore partially oxidized). The theoretical fits are compared to the experimental data collected at the Pt L_3 and Au L_3 edges in Fig. 8, with quantitative results summarized in Table III. The S^2_0 values used in the fits, which were those determined from the Pt and Au foil standards, were 0.87 and 0.83, respectively. The edge normalization factor, A, was 3.30, reflecting the higher relative Pt concentration present in this sample. The difference between the empirical threshold energies for the Pt L_3 and Au L_3 absorption edges was 358 eV.

At the Pt L_3 edge, both the Pt-O and Pt-M (M=Pt or Au) scattering paths were fit. At the Au L_3 edge, the Au-M and Pt-M overlap contributions were analyzed. It was not necessary to include an overlap contribution from the Pt-O scattering in the Au L_3 edge analysis because the amplitude of

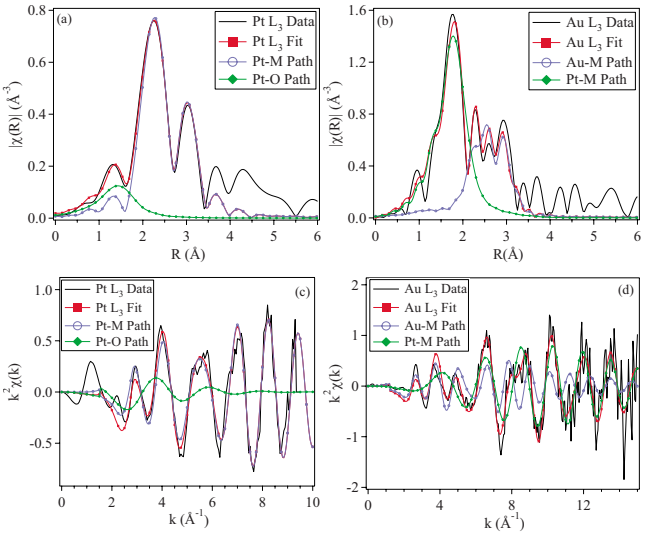

FIG. 8. (Color online) Comparison of the data and fit of the Pt-Au hybrid nanomaterial measured at room temperature and under ambient atmosphere at the Pt L_3 and Au L_3 absorption edges. (a) Fourier transform magnitude of the Pt L_3 data and fit (k =2.5–8.7 Å^{-1}, R=1.1–3.4 Å, k^2 weighted) with the Pt-M and Pt-O contributions plotted individually. (b) Fourier transform magnitude of the Au L_3 data and fit (k=2.0–14.5 Å^{-1}, R=1.1–3.2 Å, k^2 weighted) with the contributions of the individual paths represented. (c) k-space plot of Pt L_3 data, fit, and paths. (d) k-space plot of Au L_3 data, fit, and paths.

TABLE III. Results of the fit to $\chi(R)$ of the Pt and Au L_3 EXAFS using FEFF and FEFFIT for the Pt-Au nanohybrid.

Pt parameters		Au parameters	
N_{Pt}	8.0 ± 0.3	N_{Au}	9.8 ± 2.1
$\Delta E_{0,Pt}$ (eV)	9.1 ± 0.5	$\Delta E_{0,Au}$ (eV)	5.8 ± 1.6
R_{Pt} (Å)	2.756 ± 0.006	R_{Au} (Å)	2.86 ± 0.03
σ^2_{Pt} (Å^2)	0.0058 ± 0.0002	σ^2_{Au} (Å^2)	0.009 ± 0.002
$\sigma^{(3)}_{Pt}$ (Å^3)	0.00011 ± 0.00005	$\sigma^{(3)}_{Au}$ (Å^3)	0 ± 0.0003
$N_{Pt\text{-}O}$	1.1 ± 0.6		
$R_{Pt\text{-}O}$ (Å)	1.93 ± 0.05		
$\sigma^2_{Pt\text{-}O}$ (Å^2)	0.02 ± 0.01		
Pt L_3 k range (Å^{-1})	2.5–8.7	Au L_3 k range (Å^{-1})	2.0–14.5
Pt L_3 R range (Å)	1.1–3.4	Au L_3 R range (Å)	1.1–3.2

Independent points	25.9
Variables	13
Reduced χ^2	2.32
R factor	0.005

photoelectron scattering, $f^{eff}(k)$, from a low atomic number neighbor is quite small at 358 eV beyond the absorption edge, as shown in Fig. 8(c). Residual contributions, additionally, would be shifted to a sufficiently low R value upon Fourier transformation that it likely would be eliminated by the background subtraction algorithms. These assertions were verified independently by attempting to include a Pt-O contribution in the Au EXAFS; in this case no impact on the fit was found.

Consistent with the elemental segregation of the Pt-Au hybrids revealed by analytical electron microscopy, the coordination numbers determined from the EXAFS analysis differ for the two component metals. The Pt-M and Pt-O coordination numbers of 8.0 ± 0.3 and 1.1 ± 0.6, respectively, are consistent with Pt wires that are 2.3 nm in diameter and that bear a surface oxide layer on the order of a monolayer in thickness. The Au-M coordination number expected for an approximately 4.5 nm Au cuboctahedral nanocrystallite is 10.6, a geometric estimate in agreement with the observed experimental value of 9.8 ± 2.1.[35]

The Pt-Au sample exhibits Pt bond lengths that are contracted relative to the value measured for the bulk standard at the same temperature (2.772 ± 0.002 Å). However, the Au bond length in the Pt-Au hybrid is indistinguishable from the bulk standard value (2.873 ± 0.003 Å), a finding likely due to the relatively large size of the Au nanoparticles as well as the larger uncertainty in this parameter. The bond disorder in the Pt-Au hybrid follows a trend that is consistent with the above as evidenced by the mean squared relative displacements. The Pt bonds show an increased disorder compared to the bulk standard, whereas the Au bond disorder is statistically indistinguishable from the bulk value (0.0050 ± 0.0001 Å^2 for Pt and 0.0080 ± 0.0002 Å^2 for Au, measured at 293 K). The fact that this increased disorder is not as dramatic as that exhibited in the Ir-Pt nanoparticles likely derives from the larger sizes of the Pt-Au nanohybrids in this case and the more complete segregation of the component metals (which minimizes the number of heterometallic bonds contributing to the variance in bond lengths being fit by a monometallic path).

V. DISCUSSION

The results presented above for the bimetallic nanomaterials are clearly consistent with a core-shell structure for the Ir-Pt nanoparticles and a fully segregated structure for the Pt-Au hybrid nanowires. These structural characterizations were enabled by a new EXAFS analysis protocol that accounts for the absorption edge overlap of the constituent metals. The advantages of this two-edge simultaneous analysis were demonstrated first by the analysis of spectra collected from metallic standards in a stacked configuration. Improvements in the fitting results were observed at both the low- and high-energy absorption edges compared to strategies that do not utilize all of the data available in a simultaneous fit. Until now, a large number of systems of fundamental and technological relevance have been difficult to study by XAS owing to this overlap. The method reported here includes some features originally adopted by Sinfelt *et al.* in 1982 in a study of supported IrPt clusters.[29] In this early work, the Pt L_3 EXAFS spectrum was fit with the Pt EXAFS function and the Ir L_3 overlap contribution by correctly accounting for the relationship between the wave vectors associated with the two absorption edges [the role accomplished by the threshold energy correction $\Delta E_{0,Ir} - (349 \text{ eV} + \Delta E_{0,Pt})$ in the analysis described above]. However, the Ir L_3 edge was not used in the analysis which amounts to throwing out the highest quality Ir EXAFS data. The information extracted from the EXAFS spectra in this case was limited to the bond lengths, and the best fit was determined by systematically varying one parameter (R_{Ir}), letting the other parameters be determined by the fitting analysis, and then selecting the R_{Ir}

and R_{Pt} values that corresponded to the lowest fitting error for physical interpretation. This method may or may not identify the global minimum of the multidimensional fitting space. These simplifications notwithstanding the work provided an insightful treatment of the problem of edge overlap.

Since that time, other reports have described the treatment of edge overlap in a number of systems including IrPt,[37] PtAu,[38] WPt,[39] PbBi,[18,40,41] and RePt.[19] The ways in which the overlap has been addressed include (1) measuring EXAFS at the lower-energy edge only;[19,37] (2) fitting the lower-energy EXAFS and then subtracting the extrapolated fit from the second absorption edge;[40] (3) analyzing higher-energy edges (L_2 and L_1);[18,39] or (4) trying to exclude the overlap contribution from the fitting range (filtering in R space).[38,41] Limiting measurements to a single edge, particularly if the energy range is truncated, misses an opportunity for more detailed (and analytically precise) structural characterizations obtained from probing both metal coordination environments. Subtracting the extrapolated EXAFS from the first edge at least accounts for overlap but it throws away useful data which can be analyzed. Additionally, subtractive methods are likely to preclude the ability to quantify correlations between the parameters of the subtracted data and the residual data. The higher-energy L_2 and L_1 edges may not overlap with other edges but they are lower in intensity and their signal quality is less than that at the L_3 edge. Fitting around an overlap contribution has the detracting consequence that it will increase uncertainties in the fit results (as illustrated in Table I). Perhaps the most pressing unknown issue is the number of studies for which EXAFS may have been deemed unsuitable due to the closeness of the L edge energies.

There have been demonstrations of the use of element specific fluorescence detection to attenuate the problem of edge overlap, for example, using a logarithmic spiral of revolution or a bent Laue analyzer to detect only the fluorescence line of the element of interest.[42–44] These analyzers, however, are not generally applicable over a wide range of energies and thus elements of interest, suffer from lower efficiencies than ion chamber transmission or fluorescence (with Z-1 or Z-2 filters and Soller slits) detection, and require constrained detector and beam geometries.[42,43] Reports of analyses made to date using these detectors remain limited. Diffraction anomalous fine structure has been demonstrated as an elegant method of edge separation but its application for this purpose is limited to systems with crystalline order, requires that the different atomic species reside at different crystallographic sites, and is intensive in terms of data processing.[45] The first two requirements severely restrict its use in the characterization of nanomaterials, which often lack long-range order. In contrast to the above, the method described in the present paper uses available analysis packages to analyze data collected using standard equipment available at any EXAFS beamline.

VI. CONCLUSIONS

A method is described to characterize bimetallic nanomaterials by analysis of EXAFS collected from overlapping absorption edges. The validity of this method is illustrated by the analysis of spectra collected from bulk metallic standards. Its particular utility to the characterization of nanomaterials is then demonstrated with two well-characterized samples: the first, a system of Ir-Pt nanoparticles supported on γ-Al_2O_3, which are revealed to have a Ir-rich core surrounded by a Pt-rich shell with marked strain relative to the bulk metals and, the second, a Pt-Au wire-particle hybrid nanomaterial, providing a more challenging application of the method due to the low concentration of Au (both absolute and relative to Pt) and the presence of a Pt-O scattering contribution. The structural model that emerges for this second sample is one of segregated Au nanoparticles and Pt nanowires with a surface oxide layer. The multiedge simultaneous fitting analysis is broadly applicable to any combination of overlapping absorption edges and utilizes the full information content of the spectroscopy (with only a small gap at the higher-energy edge of $\sim$1.5 $Å^{-1}$). It is also easily implemented using currently available and widely used analysis packages.

ACKNOWLEDGMENTS

We gratefully acknowledge the support of this work by the U.S. DOE Grants No. DE-FG02-03ER15476 (R.G.N. and A.I.F.) and No. DE-FG02-96ER45439 (G.S.G.). This work was carried out in the Center for Microanalysis of Materials, University of Illinois, which is partially supported by the U.S. DOE Grant No. DE-FG02-91-ER45439. The use of the APS was supported by the U.S. DOE Contract No. DE-AC02-06CH11357. The use of the NSLS was supported by the U.S. DOE Contract No. DE-AC02-98CH10886. Beamline X18B at the NSLS is supported in part by the Synchrotron Catalysis Consortium, U.S. DOE Grant No. DE-FG02-05ER15688. The authors wish to acknowledge Bruce Ravel for useful discussions on this work.

[1] G. Schmid, *Nanoparticles: From Theory to Application* (Wiley-VCH, Weinheim, 2004).

[2] K. J. Klabunde, *Nanoscale Materials in Chemistry* (Wiley, New York, 2001).

[3] A. Wieckowski, E. R. Savinova, and C. G. Vayenas, *Catalysis and Electrocatalysis at Nanoparticle Surfaces* (Marcel Dekker, New York, 2003).

[4] C. W. Hills, N. H. Mack, and R. G. Nuzzo, J. Phys. Chem. B **107**, 2626 (2003).

[5] T. Huang and R. W. Murray, J. Phys. Chem. B **107**, 7434 (2003).

[6] T. Pal, A. Pal, and S. Panigrahi, in *Nanotechnology in Biology and Medicine*, edited by T. Vo-Dinh (CRC Press, Boca Raton, FL, 2007), p. 8/1.

[7] B. Coq and F. Figueras, Coord. Chem. Rev. **178-180**, 1753

(1998).
[8] C. W. Hills, M. S. Nashner, A. I. Frenkel, J. R. Shapley, and R. G. Nuzzo, Langmuir **15**, 690 (1999).
[9] D. C. Koningsberger and R. Prins, *X-Ray Absorption: Principles, Applications, Techniques of EXAFS, SEXAFS and XANES* (Wiley, New York, 1988).
[10] D. C. Koningsberger, B. L. Mojet, G. E. van Dorssena, and D. E. Ramaker, Top. Catal. **10**, 143 (2000).
[11] B. K. Teo, *EXAFS: Basic Principles and Data Analysis* (Springer-Verlag, Berlin, 1986).
[12] M. S. Nashner, D. M. Somerville, P. D. Lane, D. L. Adler, J. R. Shapley, and R. G. Nuzzo, J. Am. Chem. Soc. **118**, 12964 (1996).
[13] M. S. Nashner, A. I. Frenkel, D. Somerville, C. W. Hills, J. R. Shapley, and R. G. Nuzzo, J. Am. Chem. Soc. **120**, 8093 (1998).
[14] M. S. Nashner, A. Frenkel, D. L. Adler, J. R. Shapley, and R. G. Nuzzo, J. Am. Chem. Soc. **119**, 7760 (1997).
[15] N. Toshima and T. Yonezawa, New J. Chem. **22**, 1179 (1998).
[16] J. Batista, A. Pintar, J. P. Gomilšek, A. Kodre, and F. Bornette, Appl. Catal., A **217**, 55 (2001).
[17] B.-J. Hwang, L. S. Sarma, J.-M. Chen, C.-H. Chen, S.-C. Shih, G.-R. Wang, D.-G. Liu, J.-F. Lee, and M.-T. Tang, J. Am. Chem. Soc. **127**, 11140 (2005).
[18] W. R. Flavell, M. Mian, A. J. Roberts, J. F. Howlett, M. M. Sarker, P. L. Wincott, R. L. Bilsborrow, and G. van Dorssen, J. Mater. Chem. **7**, 357 (1997).
[19] C. G. Michel, W. E. Bambrick, R. H. Ebel, G. Larsen, and G. L. Haller, J. Catal. **154**, 222 (1995).
[20] J. A. Anderson and M. F. García, in *Catalytic Science Series*, edited by G. J. Hutchings (Imperial College Press, London, 2005).
[21] D. Bazin, C. Mottet, and G. Tréglia, Appl. Catal., A **200**, 47 (2000).
[22] L. Guczi, Catal. Today **101**, 53 (2005).
[23] V. I. Bukhtiyarov and M. G. Slin'ko, Russ. Chem. Rev. **70**, 147 (2001).
[24] H. F. Rase, *Handbook of Commercial Catalysts: Heterogeneous Catalysts* (CRC Press, Boca Raton, 2000).
[25] O. B. Yang, S. I. Woo, and Y. G. Kim, Appl. Catal., A **115**, 229 (1994).
[26] B. Ravel and M. Newville, J. Synchrotron Radiat. **12**, 537 (2005).
[27] J. J. Rehr, R. C. Albers, and S. I. Zabinsky, Phys. Rev. Lett. **69**, 3397 (1992).
[28] M. Newville, J. Synchrotron Radiat. **8**, 322 (2001).
[29] J. H. Sinfelt, G. H. Via, and F. W. Lytle, J. Chem. Phys. **76**, 2779 (1982).
[30] L. D. Menard, J. H. Kang, A. J. Sealey, G. S. Girolami, R. G. Nuzzo, and A. I. Frenkel (unpublished).
[31] X. Teng, W. Han, Q. Wang, L. Li, A. I. Frenkel, and J. C. Yang, J. Phys. Chem. C **112**, 14696 (2008).
[32] M. Newville, P. Livins, Y. Yacoby, J. J. Rehr, and E. A. Stern, Phys. Rev. B **47**, 14126 (1993).
[33] N. Seriani, W. Pompe, and L. C. Ciacchi, J. Phys. Chem. B **110**, 14860 (2006).
[34] S. Díaz-Moreno, D. C. Koningsberger, and A. Muñoz-Páez, Nucl. Instrum. Methods Phys. Res. B **133**, 15 (1997).
[35] A. I. Frenkel, C. W. Hills, and R. G. Nuzzo, J. Phys. Chem. B **105**, 12689 (2001).
[36] L. D. Menard, H. Xu, S.-P. Gao, R. D. Twesten, A. S. Harper, Y. Song, G. Wang, A. D. Douglas, J. C. Yang, A. I. Frenkel, R. W. Murray, and R. G. Nuzzo, J. Phys. Chem. B **110**, 14564 (2006).
[37] A. El Biyyadh, M. Guérin, C. Kappenstein, D. Bazin, and H. Dexpert, J. Chim. Phys. Phys.-Chim. Biol. **86**, 1751 (1989).
[38] H. M. Chen, H.-C. Peng, R. S. Liu, S. F. Hu, and L.-Y. Jang, Chem. Phys. Lett. **420**, 484 (2006).
[39] O. S. Alexeev, G. W. Graham, M. Shelef, and B. C. Gates, J. Catal. **190**, 157 (2000).
[40] J. B. Boyce, F. G. Bridges, T. Claeson, T. H. Geballe, G. G. Li, and A. W. Sleight, Phys. Rev. B **44**, 6961 (1991).
[41] Z.-u.-N. Akhtar, M. J. Akhtar, and C. R. A. Catlow, J. Mater. Chem. **4**, 1081 (1994).
[42] D. M. Pease, M. Daniel, J. I. Budnick, T. Rhodes, M. Hammes, D. M. Potrepka, K. Sills, C. Nelson, S. M. Heald, D. L. Brewe, A. I. Frenkel, I. Gregorieva, and A. Antonov, Rev. Sci. Instrum. **71**, 3267 (2000).
[43] A. J. Kropf, R. J. Finch, J. A. Fortner, S. Aase, C. Karanfil, C. U. Segre, J. Terry, G. Bunker, and L. D. Chapman, Rev. Sci. Instrum. **74**, 4696 (2003).
[44] Y. Pushkar, J. Yano, P. Glatzel, J. Messinger, A. Lewis, K. Sauer, U. Bergmann, and V. Yachandra, J. Biol. Chem. **282**, 7198 (2007).
[45] B. Ravel, C. E. Bouldin, H. Renevier, J. L. Hodeau, and J. F. Berar, Phys. Rev. B **60**, 778 (1999).